ELectronics EXpress

MS#2026XCL0119

IEICE Electronics Express, Vol.23, No.xx, 1–6

LETTER

An integrated approach for magnetostriction measurement and simulation of nanocrystalline alloys in high-frequency transformers

Xiaotong Wang[1,2], **Changgeng Zhang**[1,2,a)], **Yongjian Li**[1,2], **Hao Zhang**[1,2], **and Qingxin Yang**[1,2]

Abstract Accurately predicting the magnetostriction of nanocrystalline alloy laminations is crucial for analyzing high-frequency transformer core vibration and noise. To resolve the magnetic circuit asymmetry in existing single-yoke measurements, a high-frequency magnetostriction testing system for nanocrystalline laminations is designed with a double-yoke configuration, adopting a mirror-reflected L-shaped laser path to achieve precise measurement under high-frequency sinusoidal excitation. To overcome the limitations of traditional simulation models relying on single physical mechanisms or pure data-driven approaches, a universal dynamic magnetostriction simulation method based on the Energetic-PSO-LSTM coupled model is proposed. Comparative verification shows that at 0.5 T, the coupled model's RMSE is reduced to 0.69, significantly improving prediction accuracy and validating its reliability.

Keywords: dynamic magnetostriction properties, Energetic-PSO-LSTM coupled model, nanocrystalline alloy

Classification: Electromagnetic theory

1. Introduction

Driven by energy-efficient, lightweight power equipment demands and advances in ferromagnetic materials, nanocrystalline alloys are widely used in high-frequency transformer cores for their superior magnetic properties [1, 2]. A distinct magnetostrictive effect during magnetization [3–6] causes vibration and noise in electrical devices [7, 8], making precise property prediction critical for transformer optimization.

In magnetostriction testing, the inverse method [9–11] ignored fabrication stresses; Refs. [12–14] encountered magnetic circuit asymmetry that prevented synchronous sample characterization despite upper yoke removal. While a bonded laminated structure [15–17] addressed lamination bending, no solution has resolved single-yoke asymmetry for high-frequency nanocrystalline lamination testing. This study thus innovatively designs a dual-yoke system integrated with laser Doppler vibrometry and an L-shaped laser path to fill this gap.

[1] State Key Laboratory of Smart Power Distribution Equipment and System, Hebei University of Technology, Tianjin 300401, China

[2] Hebei Key Laboratory of Equipment and Technology Demonstration of Flexible DC Transmission, Hebei University of Technology, Tianjin 300401, China

[a)] changgeng.zhang@hebut.edu.cn

DOI: 10.1587/elex.23.20260119
Received February 9, 2026
Accepted February 24, 2026
Publicized Xxxx xx, xxxx
Copyedited Xxxx xx, xxxx

In simulation research, modified J-A models [18, 19] improved precision but remained static, limiting engineering use; dynamic J-A models [5, 20, 21] faced computational complexity and convergence issues. Although the dynamic Energetic-J-A-S model [22] showed promise, current models fail to balance physical interpretability and prediction accuracy for nanocrystalline alloys.

To address these dual gaps, this study develops the aforementioned dual-yoke testing system and proposes an Energetic-Particle Swarm Optimization-Long Short-Term Memory (Energetic-PSO-LSTM) hybrid model that synergizes physical mechanisms and data-driven algorithms. Numerical simulation and experiments verify the method's effectiveness and accuracy.

2. Energetic-PSO-LSTM coupled magnetostriction model

To address the insufficient accuracy of the single Energetic physical model in magnetostrictive calculations, this paper proposes an Energetic-PSO-LSTM coupled algorithm. By applying PSO-LSTM to correct the deviation in the Energetic model's computational results, the accuracy is enhanced. The final expression for magnetostriction derived from the coupled model calculations is:

$$\lambda_{\text{coupled},t} = \lambda_{\text{Energetic},t} + \Delta\lambda_t \tag{1}$$

where, $\lambda_{\text{coupled},t}$ denotes the magnetostrictive value computed by the proposed coupling model at time t, $\lambda_{\text{Energetic},t}$ denotes the magnetostrictive value computed by the Energetic model at time t, and $\Delta\lambda_t$ denotes the magnetostrictive correction value computed by the PSO-LSTM model at time t.

Figure 1 presents the flowchart of the proposed coupling model. This paper first simulates magnetostrictive curves based on the Energetic model, with the workflow depicted in the left column of the figure. To bring simulation values closer to measured values, the results calculated by the Energetic model are fed into the PSO-LSTM for further computation and error correction. The PSO-LSTM computation process is shown in the right column of the figure. The final output values from the coupled model are compared with experimental data to conduct error analysis.

2.1 Dynamic energetic original model

The static Energetic hysteresis model is shown as [23, 24]:

This work is licensed under a Creative Commons Attribution NonCommercial, No Derivatives 4.0 License.
Copyright © 2026 The Institute of Electronics, Information and Communication Engineers

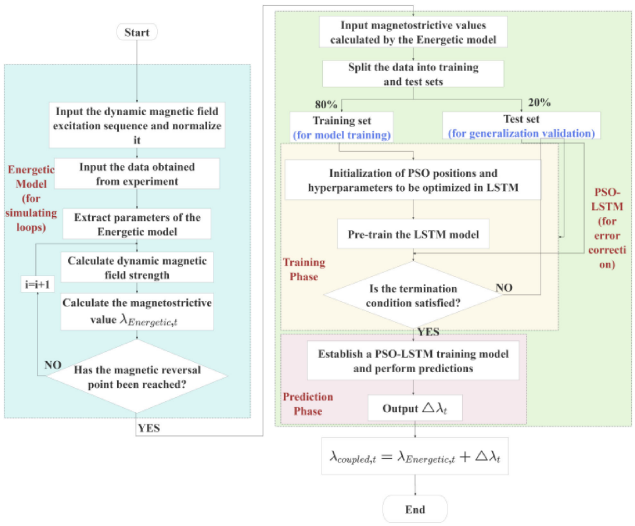


Fig. 1 Flowchart of the Energetic-PSO-LSTM coupled model.

$$H_{\mathrm{sta}} = \mathrm{sgn}(b)H_{\mathrm{r}} + \mathrm{sgn}(b - b_0)H_{\mathrm{ir}} \tag{2}$$

$$H_{\mathrm{ir}} = \mathrm{sgn}(b - b_0) \times \left(\frac{k}{B_{\mathrm{s}}} + c_{\mathrm{r}}H_{\mathrm{r}}\right)\left[1 - \kappa \exp\left(-\frac{q}{\kappa}|b - b_0|\right)\right] \tag{3}$$

where H_{sta} is the static magnetic field strength; H_{r} is the reversible magnetic field strength; H_{ir} is the irreversible magnetic field strength; b is normalized magnetic field strength; B_{s} is saturated magnetic flux density; b_0 is the previous magnetization reversal point; k is the hysteresis loss coefficient; μ_0 is the magnetic permeability of free space; c_{r} is the adaptive domain size scaling coefficient; κ is the inversion function; q is the coefficient related to the pinning density; sgn(·) is the sign function. The expressions for the reversible magnetic field strength and the reversal function are respectively:

$$H_{\mathrm{r}} = h_0\{[(1+b)^{1+b}(1-b)^{1-b}]^{\frac{g}{2}} - 1\} \tag{4}$$

$$\kappa = 2 - \kappa_0 \exp\left(-\frac{q}{\kappa_0}|b - b_0|\right) \tag{5}$$

where h_0 is the proportionality coefficient related to the saturation magnetic field; g is the adaptive coefficient related to the anisotropy of the soft magnetic material; κ_0 is the value of the previous magnetization reversal point.

According to the loss separation theory [25, 26] and field separation technology [27], the expression for the dynamic Energetic hysteresis model is:

$$H_{\mathrm{dyn}} = H_{\mathrm{sta}} + H_{\mathrm{c}} + H_{\mathrm{e}} \tag{6}$$

$$H_{\mathrm{c}} = \frac{\sigma d^2}{12}\int_0^T \left(\frac{dB}{dt}\right)^2 dt \tag{7}$$

$$H_{\mathrm{e}} = \sqrt{\sigma S G V_0}\int_0^T \left|\frac{dB}{dt}\right|^{3/2} dt \tag{8}$$

where $\mathrm{H_{dyn}}$ is the dynamic magnetic field strength; H_{c} represents classical eddy current magnetic field strength; H_{e} denotes the excess magnetic field strength; σ denotes the electrical conductivity; d represents the thickness; T is the magnetization period; S signifies the cross-sectional area along the magnetization direction; G is a dimensionless coefficient with a value of 0.1375; V_0 is a statistical parameter characterizing the local magnetic field distribution.

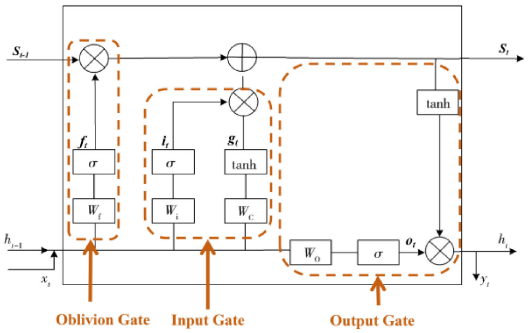


Fig. 2 LSTM structure.

The expression for magnetostriction using dynamic Energetic original model is obtained as follows:

$$\lambda_{\mathrm{Energetic},t} = \lambda_{\mathrm{s}}\left(\frac{3}{2}\left(\frac{\frac{B}{\mu_0} - H_{\mathrm{dyn}}}{M_{\mathrm{s}}}\right)^2 - \frac{1}{2}\right) \tag{9}$$

2.2 PSO-LSTM dynamic magnetostrictive model

The core function of PSO-LSTM is to correct simulation errors in the Energetic model. The dynamic magnetostrictive exhibits significant temporal dependence and strong nonlinear hysteresis characteristics. LSTM, with its precise ability to capture long-term temporal dependencies and robust nonlinear mapping capabilities, can effectively fit this dynamic process. The LSTM structure diagram is shown in Fig. 2.

The model input utilizes the dynamic magnetic induction intensity B time series obtained from the Energetic model simulation described earlier. The output represents the correction value for the corresponding λ at each time point. After normalization to eliminate dimensional differences, the data is divided into training and test sets in an 8:2 ratio. The recursive equation for the forgetting gate is:

$$f_t = \sigma(W_f \cdot [\Delta\lambda_{t-1}, B_t] + b_f) \tag{10}$$

The recursive equation for the input gate is:

$$i_t = \sigma(W_i \cdot [\Delta\lambda_{t-1}, B_t] + b_i) \tag{11}$$

$$\tilde{C}_t = \tanh(W_C \cdot [\Delta\lambda_{t-1}, B_t] + b_C) \tag{12}$$

The recursive equation for the output gate is:

$$o_t = \sigma(W_o \cdot [\Delta\lambda_{t-1}, B_t] + b_o) \tag{13}$$

$$C_t = f_t * C_{t-1} + i_t * \tilde{C}_t \tag{14}$$

$$\Delta\lambda_{\mathrm{t}} = o_t * \tanh(C_t) \tag{15}$$

Where, f_t is the forgetting gate, i_t is the input gate, o_t is the output gate, $\Delta\lambda_{\mathrm{t-1}}$ is the output of the previous moment, B_t is the input of the current moment, W_f, W_i, W_C, W_o is the weight matrix, b_f, b_i, b_C, b_o is the bias vector, $\tilde{C}_t$ is the post-selected memory state of the current moment, and C_t is the memory state of the current moment.

To enhance the prediction accuracy and stability of the LSTM network, we optimize its key hyperparameters using PSO algorithm [28]. Specifically, the PSO is configured

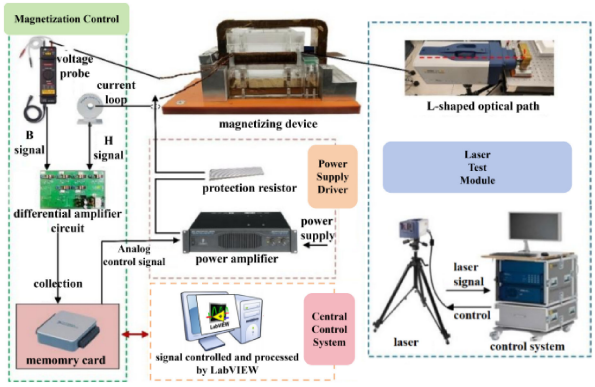


Fig. 3 Testing system diagram.

with 30 particles, a maximum of 50 iterations, an inertia weight range of 0.8–1.2, and learning factors set to 2.

Each particle constantly updates its position and velocity over time. The update formula is as follows:

$$V_i^{(k+1)} = \omega(t)V_i^{(k)} + c_1 r_1[P_{best,i}(\lambda) - X_i^{(k)}] + c_2 r_2[G_{best,i}(\lambda) - X_i^{(k)}] \tag{16}$$

$$X_i^{(k+1)} = V_i^{(k+1)}(\lambda) + X_i^{(k)} \tag{17}$$

$$\omega(t) = \frac{(t_{\max} - t)(\omega_{\max} - 1)}{(t_{\max} - 1) + \omega_{\min}} \tag{18}$$

where $P_{best,i}(\lambda)$ is the individual optimal solution; $G_{best,i}(\lambda)$ is the global optimal solution; $\omega(t)$ is the inertia weight; c_1 and c_2 are the learning factors at the time when the particle is updated; r_1 and r_2 are the random number uniformly distributed in the range 0–1.

3. Testing and analysis of magnetostriction properties in nanocrystalline alloys

In this study, a high-frequency magnetostriction measurement system for laminated nanocrystalline alloy 1K107B is developed using a dual-yoke magnetic circuit structure. Combined with a dual-yoke magnetic property tester and laser Doppler vibrometry (Fig. 3), following IEC 60404-2 [29, 30], it provides a reliable experimental platform for studying high-frequency dynamic magnetostriction in nanocrystalline alloys.

3.1 Test apparatus structure for magnetostriction testing of optical paths

To avoid the obstruction of optical paths inherent in traditional direct laser projection methods, this paper employs a reflective mirror to design an L-shaped optical path, as shown in Fig. 4. During testing, one end of the sample is fixed while the laser source is positioned at the opposite end. The laser beam is projected vertically along the sample's length into a 45° reflective mirror, where it is reflected toward the optical target. The target then reflects the laser beam back along its original path to the laser source.

For accurate magnetostriction measurement, the custom L-shaped optical path requires optimized reflector selection and precise position/angle calibration (Fig. 5). An isosceles right triangular prism is mounted on a perpendicular sandwich support plate to optimize the sample-reflector vertical distance. Additional measures include suspending the magnetic yoke to avoid excess pressure and lining the sample contact surface with low-friction PTFE film to minimize gravity-induced and frictional interference.

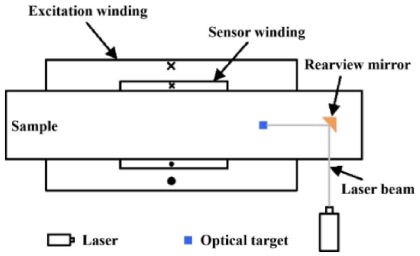


Fig. 4 Schematic diagram of L-shaped optical path.

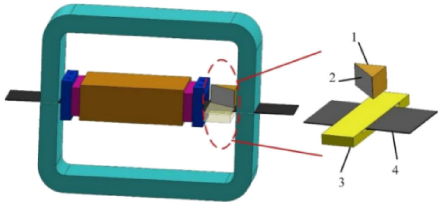


Fig. 5 Schematic of configuration of reflection components (1. mirror base; 2. mirror; 3. support plate; 4. specimen).

Table I Specification parameters of nanocrystalline alloy laminate.

Parameters	Value
Length/mm	162
Width/mm	30
Thickness (10 laminated sheets)/μm	20
Density/ ($kg \cdot m^{-3}$)	7200
Electrical Conductivity/($S \cdot m^{-1}$)	7.69×10^4
Young's modulus/GPa	120
Poisson ratio	0.3

3.2 Analysis of magnetostriction properties of nanocrystalline alloys under sinusoidal excitation

The nanocrystalline alloy sample selected for testing is the 1K107B model, with specifications as shown in Table I. Due to the brittle nature and excessive thinness of individual annealed nanocrystalline alloy sheets, issues such as brittle fracture, difficulty in clamping, and positional shifts may occur during measurement, affecting the experimental process and accuracy. Therefore, ten sheets of nanocrystalline alloy were laminated together for measuring their magnetostriction properties.

Figure 6 depicts the magnetostriction butterfly curve of nanocrystalline alloy laminations under a 5 kHz sinusoidal magnetic field. This curve features symmetric left/right loop areas and upward-opening wings; magnetostriction is dominated by tensile strain, where the positive/negative half-axes correspond to tensile/compressive strain, respectively.

Figure 7 depicts the uniaxial magnetostriction curves of nanocrystalline alloy laminations under a 5 kHz excitation field. The magnetostriction peak-to-peak value (λpp) clearly rises with increasing magnetic flux density in a nonlinear pattern, with a marked surge occurring at relatively high flux densities.

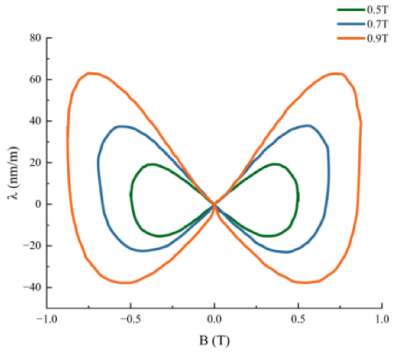


Fig. 6 Magnetostriction of nanocrystalline alloy laminations under 5 kHz sine excitation.

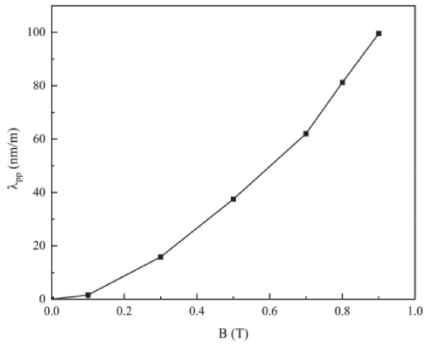


Fig. 7 Magnetostriction single-value curve of 5 kHz nanocrystalline alloy laminations.

Under sinusoidal excitation, magnetostriction and magnetic flux density exhibit a nonlinear relationship, with the magnetostriction effect intensifying at higher flux densities. At low flux densities, the external magnetic field only induces reversible domain wall displacement, which experiences slight hindrance from the uniform microstructure and thus results in a gentle increase in magnetostriction. As the flux density approaches saturation, magnetic domains rotate rapidly toward the magnetic field direction, leading to a sharp surge in magnetostriction peak-to-peak value.

4. Model simulation and accuracy verification

4.1 Magnetostriction prediction results and analysis

The Energetic model parameters for the saturated magnetostriction curve of nanocrystalline 1K107B are shown in Table II.

To verify the predictive performance of the developed model, it is benchmarked against the original Energetic model (Energetic-OD) and experimental measurements.

Figure 8 shows the magnetostriction curve of nanocrystalline alloy laminations under 5 kHz sinusoidal excitation at 0.5 T. The original Energetic model exhibits suboptimal saturation-region simulation (19 nm/m peak elongation, 14 nm/m peak contraction); feeding its outputs into the PSO-LSTM model to form the Energetic-PSO-LSTM coupled model markedly improved performance (20 nm/m peak elongation, 15 nm/m peak contraction), while experimental measurements yielded 21 nm/m peak elongation and 17 nm/m peak contraction.

Figure 9 presents the magnetostriction butterfly curve of nanocrystalline alloy laminations under 5 kHz sinusoidal excitation with a 0.7 T magnetic flux density. The standalone Energetic model calculates a maximum elongation strain of 38 nm/m and maximum contraction strain of 23 nm/m, while the measured values are 38 nm/m and 25 nm/m respectively. The curve maintains bilateral symmetry with a butterfly shape, and the contraction strain from the single Energetic model shows greater deviation from the measured data. The Energetic-PSO-LSTM coupled model yields approximately 35 nm/m maximum elongation strain and 25 nm/m maximum contraction strain.

Figure 10 presents the magnetostriction butterfly curve of nanocrystalline alloy laminations under 5 kHz sinusoidal excitation with a 0.9 T magnetic flux density amplitude, where the material reaches saturation. The standalone Energetic model predicts a maximum elongation strain of 62 nm/m and contraction strain of 30 nm/m, while the measured values are 62 nm/m and 38 nm/m respectively. Corrected by the PSO-LSTM algorithm, the Energetic-PSO-LSTM coupled model yields approximately 62.5 nm/m

Table II Energetic model parameters for saturated magnetostriction curve.

Parameters	Value
k (a.u.)	2.5
h_0 (μA/m)	23
g (a.u.)	25.6
q (a.u.)	6.8
Cr (a.u.)	2.3e-10

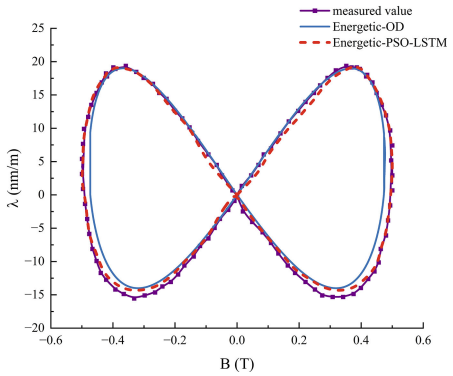


Fig. 8 Magnetostriction prediction comparison (5 kHz, B=0.5 T).

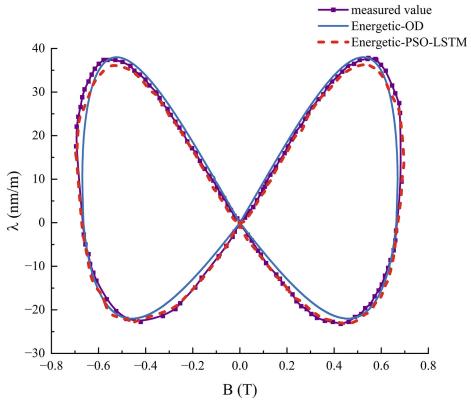


Fig. 9 Magnetostriction prediction comparison (5 kHz, B=0.7 T).

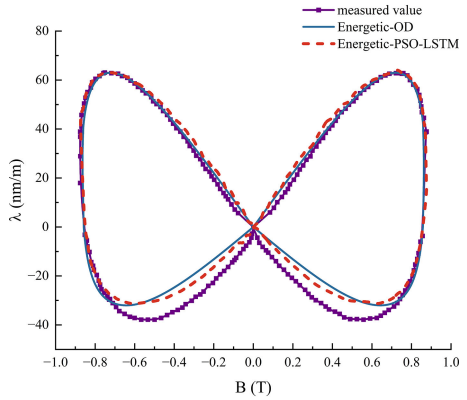


Fig. 10 Magnetostriction prediction comparison (5 kHz, B=0.9 T).

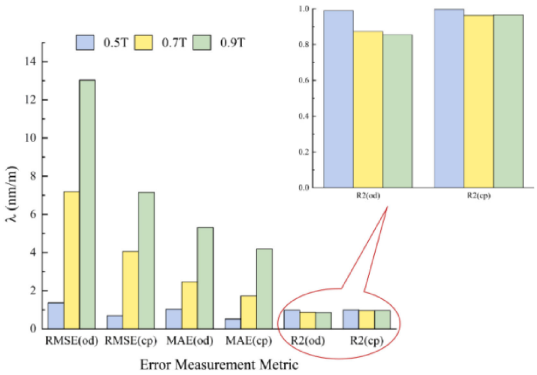


Fig. 11 Comparison of model errors.

maximum elongation and 32.5 nm/m maximum contraction. Despite residual errors in contraction strain simulation, the coupled model shows closer agreement with experimental data than the single Energetic model.

With increasing magnetic flux density, the magnetostriction deformation exhibits more pronounced elongation and contraction trends. Simulation results demonstrate that the proposed method can accurately capture the variation characteristics of the magnetostriction curve. Furthermore, the simulated magnetostriction curve generated by this method aligns more closely with both traditional methods and experimental measurements, validating the effectiveness of the proposed approach.

4.2 Error analysis

To rigorously verify the reliability of model predictions, root mean square error (RMSE), mean absolute error (MAE), and coefficient of determination (R^2) are selected for quantitative evaluation of model performance.

Model error comparison (Fig. 11) shows that the proposed Energetic-PSO-LSTM coupled model achieves higher R^2 and lower RMSE/MAE across magnetic flux densities, indicating superior fitting performance. At 0.5 T, R^2 increased by 0.74% (from 0.9903 to 0.9976), RMSE decreased by 49.64% (from 1.37 to 0.69), and MAE by 50% (from 1.04 to 0.52). The coupled model thus outperforms the original Energetic model with strong generalization.

5. Conclusion

This study develops a testing system to characterize the dynamic magnetostriction of nanocrystalline alloy laminations under sinusoidal excitation. Based on magnetization theory and experimental data, an Energetic-PSO-LSTM coupled prediction model is proposed and validated against test results. Key conclusions are as follows:

(1) Harnessing laser measurement advantages, a reflector-integrated laser optical path enables precise quantification of nanocrystalline alloy magnetostriction under high-frequency sinusoidal excitation.

(2) The proposed model synergizes magnetostriction's intrinsic physical mechanisms with data-driven fitting capacity, yielding excellent extensibility and universality for predicting magnetostriction in diverse magnetic materials under varying conditions.

(3) Simulated-experimental comparisons confirm the model's superior fitting accuracy: the original Energetic model has an RMSE of 1.37, while the coupled model achieves a markedly lower value of 0.69 at 0.5 T, representing a significant improvement in prediction precision.

Acknowledgments

This work was supported in part by the National Natural Science Foundation of China, (No. 52277008, 52130710), and Natural Sciences foundation of Hebei Province, China (E2023202050).

References

[1] W. Ge, *et al.*: "Analysis of strong magnetic environment interference of inspection rotary wing UAV," IEICE Electron. Express **20** (2023) 20230321 (DOI: 10.1587/elex.20.20230321).

[2] H. Liu, *et al.*: "Calculation and experimental verification of core loss in high frequency transformer under non-sinusoidal excitation," Trans. China Electrotech. Soc. **38** (2023) 1217.

[3] Z. Guo, *et al.*: "Dynamic hysteresis model of grain-oriented ferromagnetic material using neural operators," arxiv preprint (2025) arXiv:2504.04863.

[4] Z. Wang, *et al.*: "Study of magnetostrictive characteristics based on dynamic J–A model under DC bias," IEEE Trans. Magn. **60** (2024) 7301604 (DOI: 10.1109/TMAG.2024.3462497).

[5] H. Zhang, *et al.*: "Magnetic properties simulation of electrical steel sheet based on recurrent neural network," IEEE Trans. Magn. **60** (2023) 7300304 (DOI: 10.1109/TMAG.2023.3316753).

[6] K. Roppert, *et al.*: "Magnetoelastic vector hysteresis modelling for electromagnetic devices: A combination of a multiscale model with the energy-based hysteresis framework," IEEE Trans. Magn. **61** (2025) 7300414 (DOI: 10.1109/TMAG.2025.3584819).

[7] T. Chen, *et al.*: "Study on electromagnetic vibration characteristics of anode saturable reactor considering anisotropic properties," IEEE Trans. Instrum. Meas. **74** (2025) 6010312 (DOI: 10.1109/TIM.2025.3602530).

[8] Y. Cai, *et al.*: "Magnetostriction vibration and acoustic noise in motor stator cores," IEEE Trans. Ind. Appl. **60** (2024) 6066 (DOI: 10.1109/TIA.2024.3384335).

[9] P. Zhang and L. Li: "Vibration and noise characteristics of high-frequency amorphous transformer under sinusoidal and non-sinusoidal voltage excitation," Int. J. Electr. Power Energy Syst. **123** (2020) 106298 (DOI: 10.1016/j.ijepes.2020.106298).

[10] B. Chen, *et al.*: "Measurement and analysis of vibration characteristics of nanocrystalline magnetic core under symmetrical/asymmetrical waveforms," COMPEL-Int. J. Comput. Math. Electr. Electronic Eng. **42** (2023) 718 (DOI: 10.1108/COMPEL-08-2022-0294).

[11] S. Wu, *et al.*: "Analytical model for predicting vibration due to magnetostriction in axial flux permanent magnet machines with

amorphous metal cores," IEEE Trans. Magn. **53** (2017) 1 (DOI: 10.1109/TMAG.2017.2686322).

[12] M. Hirano, *et al.*: "A study on measurement of magnetostriction of silicon steel sheet by laser displacement meter," J. Magn. Magn. Mater. **254–255** (2003) 43 (DOI: 10.1016/S0304-8853(02)00741-2).

[13] H. J. Stanbury: "International standards applied to magnetic alloys and steels," IEEE Trans. Magn. **46** (2010) 274 (DOI: 10.1109/TMAG.2009.2033461).

[14] S. Siebert, *et al.*: "Establishment of the standard method of magnetostriction measurement of grain-oriented electrical steel strip and sheet," J. Magn. Magn. Mater. **565** (2023) 170295 (DOI: 10.1016/j.jmmm.2022.170295).

[15] X. Zhu, *et al.*: "Effect of uniaxial stress on magnetic property of laminated amorphous sheets up to kilohertz range," AIP Adv. **14** (2024) 015150 (DOI: 10.1063/9.0000696).

[16] L. H. Zhu, *et al.*: "Effect of clamping force on magnetic properties and core vibration of amorphous alloys," Proc. CSEE **40** [22] (2020) 8155.

[17] A. Raghunathan, *et al.*: "Application of Jiles-Atherton model to stress induced magnetic two-phase hysteresis," IEEE Trans. Magn. **49** (2013) 3187 (DOI: 10.1109/TMAG.2013.2243823).

[18] L. Daiyan, *et al.*: "Modeling of magnetostrictive characteristics in an electrical steel sheet based on the JA model and its experimental verification," Trans. China Electrotech. Soc. **37** (2022) 5081.

[19] Z. Liu, *et al.*: "Measurement and modeling of coupled magnetic hysteresis and magnetostrictive properties in core silicon steel," Adv. Technol. Electr. Eng. Energy **43** [05] (2024) 1 (DOI: 10.12067/ATEEE2310079).

[20] Y. Li, *et al.*: "A dynamic magnetostriction model of grain-oriented sheet steels based on Becker–Döring crystal magnetization model and Jiles–Atherton theory of magnetic hysteresis," IEEE Trans. Magn. **56** (2020) 1 (DOI: 10.1109/TMAG.2019.2953887).

[21] C. Rong, *et al.*: "Analysis and numerical solution of dynamic Jiles–Atherton model applied to hysteresis modeling for giant magnetostrictive materials," Eng. Comput. **39** (2022) 1451 (DOI: 10.1108/EC-03-2021-0141).

[22] H. Chen, *et al.*: "Simulation of dynamic magnetostriction characteristics of electrical steel sheet based on energetic and the improved Jiles-Atherton-Sablik models," Proc. CSEE **44** [2] (2024) 848.

[23] R. Liu and L. Li: "Parameter extraction for energetic hysteresis model based on the hybrid algorithm of simulated annealing and Levenberg-Marquardt," Proc. CSEE **39** (2019) 875.

[24] H. Hauser: "Energetic model of ferromagnetic hysteresis: Isotropic magnetization," J. Appl. Phys. **96** (2004) 2753 (DOI: 10.1063/1.1771479).

[25] G. Bertotti: "Physical interpretation of eddy current losses in ferromagnetic materials theoretical considerations," J. Appl. Phys. **57** (1985) 2110 (DOI: 10.1063/1.334404).

[26] A. Ravichandran, *et al.*: "Monte Carlo model to determine eddy currents in 3D winding configurations with and without ferromagnetic materials," Comput. Mech. **76** (2025) 769 (DOI: 10.1007/s00466-025-02625-1).

[27] M. Hamimid, *et al.*: "Dynamic formulation for energetic model compared with hybrid magnetic formulation of ferromagnetic hysteresis," Int. J. Numer. Model. **30** (2017) e2225 (DOI: 10.1002/jnm.2225).

[28] W. Ge and X. Wang: "PSO–LSTM–Markov coupled photovoltaic power prediction based on sunny, cloudy and rainy weather," J. Electr. Eng. Technol. **20** (2025) 935 (DOI: 10.1007/s42835-024-02051-y).

[29] B. Chen, *et al.*: "Simulation of dynamic hysteresis characteristics of high frequency transformer core under non-sinusoidal excitation," Proc. CSEE **44** [13] (2024) 5420.

[30] X. Xu, *et al.*: "Hysteresis and loss characteristics of Fe-based nanocrystalline alloys based on a novel variable-temperature dynamic Jiles–Atherton hysteresis model," J. Phys. D Appl. Phys. **57** (2023) 095001. (DOI: 10.1088/1361-6463/ad0fbc).